

Scandium and chromium in the strontium filament in the Homunculus of η Carinae

M. A. Bautista,^{1*} C. Ballance,² T. R. Gull,³ H. Hartman,⁴ K. Lodders,⁵ M. Martínez⁶ and M. Meléndez^{3,7}

¹Department of Physics, Virginia Polytechnic and State University, Blacksburg, VA 24061, USA

²Department of Physics, Rollins College, Winter Park, FL 32789, USA

³Code 667, NASA Goddard Space Flight Center, Greenbelt, MD 20771, USA

⁴Lund Observatory, Lund University, Box 43, SE-221 00 Lund, Sweden

⁵Planetary Chemistry Laboratory, Department of Earth and Planetary Sciences and McDonnell Center for the Space Sciences, Washington University, Saint Louis, MO 63130, USA

⁶Centro de Física, IVIC, PO Box 21827, Caracas 1020A, Venezuela

⁷Institute for Astrophysics and Computational Sciences, Department of Physics, The Catholic University of America, Washington, DC 20064, USA

Accepted 2008 November 13. Received 2008 November 10; in original form 2008 July 16

ABSTRACT

We continue a systematic study of chemical abundances of the *strontium filament* found in the ejecta of η Carinae. To this end we interpret the emission spectrum of Sc II and Cr II using multilevel non-local thermodynamic equilibrium models. Since the atomic data for these ions were previously unavailable, we carry out *ab initio* calculations of radiative transition rates and electron impact excitation rate coefficients. The observed spectrum is consistent with an electron density of the order of 10^7 cm^{-3} and a temperature between 6000 and 7000 K, conditions previously determined from [Ni II], [Ti II] and [Sr II] diagnostics. The observed spectrum indicates an abundance of Sc relative to Ni more than 40 times the solar value, while the Cr/Ni abundance ratio is roughly solar. Various scenarios of depletion and dust destruction are suggested to explain such abnormal abundances.

Key words: atomic data – atomic processes – line: formation – stars: abundances.

1 INTRODUCTION

η Carinae is a massive binary system that exhibits characteristics of a luminous blue variable (LBV; Damiani 1997; Davidson & Humphreys 1997). During the 1840s η Carinae went through the Great Eruption event that ejected a neutral, bipolar shell structure with intervening skirt called the Homunculus. The total mass in such a structure is estimated in more than $12 M_{\odot}$ based upon the normal interstellar gas to dust mass ratio (Smith et al. 2003). A lesser event in the 1890s produced the Little Homunculus, an ionized bipolar structure and skirt located within a few arcseconds from the Homunculus. The mass of the Little Homunculus is estimated to be $0.5 M_{\odot}$ (Ishibashi et al. 2003). Ionized structures external to the Homunculus (Davidson et al. 1986) show strong nitrogen and helium enhancement with virtually no carbon or oxygen. A few tenths of arcsecond of η Carinae (hundreds of au) are the Weigelt blobs (partially ionized structures) whose spectra are consistent with 100-fold depletion of carbon and oxygen relative to solar abundances (Verner et al. 2002; Verner, Bruhweiler & Bull 2005). These abundances are consistent with ejecta originating from a star at the end

of the hydrogen burning phase, provided that the initial stellar mass was over $60 M_{\odot}$ (Meynet & Maeder 2002).

Hillier et al. (2001, 2006) modelled the wind of η Carinae A and confirmed the large underabundances of carbon and oxygen and overabundance of nitrogen. The models could not clearly determine the abundance of helium relative to hydrogen, but enhancements of helium as much as tenfold were possible.

The *Hubble Space Telescope* (HST)/Space Telescope Imaging Spectrograph (STIS) spectra of the strontium filament indicate a chemical composition very different from solar. Located about 1.5 arcsec to the north-east of η Carinae and moving towards the observer at -100 km s^{-1} , the strontium filament lies in the skirt part of the Homunculus and the Little Homunculus. It was originally identified by [Sr II] emission lines in the red near hydrogen $H\alpha$ (Zethson et al. 2001). No emission lines of hydrogen or helium are present. Only weak [C I] emission is identified among the light elements, but hundreds of emission lines from iron peak elements are present, including Ca II, Sc II, Ti II, V II, Cr II, Fe II and Ni II. Well over 200 Ti II lines were identified between 2500 and 10 400 Å (Hartman et al. 2004). The radiation exciting this filament seems devoid of Lyman continuum photons through attenuation by intervening gas.

The origin of the Sr II emission in the filament was studied by Bautista et al. (2002), where we diagnosed the physical conditions of

*E-mail: bautista@vt.edu

the emitting region to be $N_e = 10^7 \text{ cm}^{-3}$, and a continuum radiation flux that can be modelled by a 35 000 K blackbody diluted by a factor $w \approx 10^{-9}$. Later, in Bautista et al. (2006) we analysed the [Ni II] and [Ti II] emission from the filament and confirmed the previous diagnostics. In addition, we constrained the electron temperature of the gas to $7000 \pm 1000 \text{ K}$. Surprisingly, this study yielded a Ti/Ni gas abundance ratio that is ~ 40 times the solar value.

In this paper we continue our study of the physical conditions of the filament and its chemical composition from the neutral and singly ionized iron-peak species observed in the *HST*/STIS spectrum. We study the excitation mechanisms of Sc II and Cr II emission lines. To do that, we calculate radiative transition rates and electron impact collision strengths for these species using ‘state-of-the-art’ atomic physics methods. Then, we calculate the gas phase abundance of Sc and Cr in the observed region.

2 ATOMIC DATA AND ATOMIC MODELS FOR SC II AND CR II

For Sc II and Cr II complete sets of radiative transition rates and collision strengths are unavailable, thus large calculations of atomic data for this ion were carried out within the present work.

2.1 Radiative data for Sc II and Cr II

We calculated radiative transition rates for dipole allowed and forbidden transitions of Sc II and Cr II using the atomic structure code AUTOSTRUCTURE (Badnell 1986). This code is based on the program SUPERSTRUCTURE originally developed by Eissner, Jones & Nussbaumer (1974). In this approach the wavefunctions are written as a configuration interaction expansion of the type

$$\psi_i = \sum_j c_{ji} \phi_j, \quad (1)$$

where the coefficients c_{ji} are chosen so as to diagonalize $\langle \psi_j | H | \psi_i \rangle$, where H is the Hamiltonian and the basic functions ϕ_j are constructed from one-electron orbitals generated using the Thomas–Fermi–Dirac–Amaldi model potential (Eissner & Nussbaumer 1969). λ_{nl} scaling parameters for each nl orbital are optimized by minimizing a weighted sum of energies. The configuration representation and scaling parameters used in this work are listed in Tables 1 and 2 for Sc II and Cr II, respectively.

Semi-empirical corrections take the form of term energy corrections (TEC). By considering the relativistic wavefunction, ψ_i^r , in a

Table 1. Sc II configurations and scaling parameters.

| |
|--|
| Spectroscopic configurations |
| $3d^2, 3d 4s, 3d 4p, 4s^2$ |
| Correlation configurations |
| $3d 4d, 3d 5s, 3d 5p, 3d 4f, 3d 6s, 4s^2, 4s 4p, 4s 4d,$ |
| $4s 5s, 4s 5p 4s 4f, 4s 6s, 4p^2 4p 4d, 4p 5s, 4p 5p$ |
| $4p 4f, 4p 6s, 4d^2 4d^2, 4d 5p 4d 4f, 4d 6s, 5s^2,$ |
| $5s 5p, 5s 4f, 5s 6s, 5p^2, 5p 4f, 5p 6s, 4f^2, 4f 6s,$ |
| $6s^2$ |
| λ_{nl} |
| 1.43670(1s), 1.1185(2s), 1.0612(2p), 1.1024(3s), 1.0924(3p), |
| 1.0709(3d), 1.1183(4s), 1.1809(4p), 1.4886(4d), 1.6872(5s), |
| 1.3200(5p), |
| 2.1200(4f), 3.6200(6s) |

Table 2. Cr II configurations and scaling parameters.

| |
|---|
| Spectroscopic configurations |
| $3s^2 3p^6 3d^5, 3s^2 3p^6 3d^4 4s, 3s^2 3p^6 3d^4 4p, 3s^2 3p^6 3d^3 4s^2,$ |
| $3s^2 3p^6 3d^3 4s 4p$ |
| Correlation configurations |
| $3s^2 3p^6 3d^4 4d, 3s^2 3p^6 3d^4 5s, 3s^2 3p^6 3d^4 5d, 3s^2 3p^5 3d^4 4s^2,$ |
| $3s^2 3p^4 3d^5 4s^2, 3s^2 3p^3 3d^6 4s^2, 3s^2 3p^6 3d^4 4d, 3s^2 3p^5 3d^5 4d,$ |
| $3s^2 3p^5 3d^5 4s, 3s^2 3p^5 3d^5 4p, 3s 3p^5 3d^6 4s, 3s 3p^4 3d^6 4s^2,$ |
| $3s 3p^5 3d^5 4s^2, 3s 3p^5 3d^6 4p, 3s 3p^6 3d^5 4s, 3s 3p^6 3d^4 4s^2,$ |
| $3s 3p^6 3d^5 4p, 3p^6 3d^6 4s, 3p^6 3d^6 4p, 3p^6 3d^5 4s^2,$ |
| $3p^5 3d^6 4s^2$ |
| λ_{nl} |
| 1.43260(1s), 1.12940(2s), 1.07230(2p), 1.09330(3s), 1.07830(3p), |
| 1.08340(3d), 1.08990(4s), 1.06500(4p), 1.49950(4d), $-1.17370(5s),$ |
| $-0.54540(5d)$ |

perturbation expansion of the non-relativistic functions ψ_i^{nr} ,

$$\psi_i^r = \psi_i^{\text{nr}} + \sum_{j \neq i} \psi_j^{\text{nr}} \frac{\langle \psi_j^{\text{nr}} | H_{1b} + H_{2b} | \psi_i^{\text{nr}} \rangle}{E_i^{\text{nr}} - E_j^{\text{nr}}}, \quad (2)$$

a modified H_{nr} is constructed with improved estimates of the differences $E_i^{\text{nr}} - E_j^{\text{nr}}$ so as to adjust the centres of gravity of the spectroscopic terms to the experimental values. Tables 3 and 4 compare the observed energies, averaged over fine structure, from Johansson & Litzén (1980) and compiled in the NIST v.3.1.2 energy levels data base (Ralchenko et al. 2007), the computed *ab initio* term energies, and the computed energies after TEC corrections for Sc II and Cr II, respectively. The overall agreement between *ab initio* energies and experimental values is typically within 10 per cent for Sc II and 15 per cent for Cr II. This is reasonable considering the complexity of the systems. These energies are very much improved by the TEC technique.

A consistency check on the accuracy of the wavefunctions can be obtained by comparing computed *gf* values in the length and velocity gauges of the dipole operator. Such comparisons are presented in Fig. 1 for 130 and 1569 transitions of Sc II and Cr II, respectively. The observed dispersion here is reasonable small (< 26 and < 29 per cent for Sc II and Cr II, respectively, for *gf* values greater than unity) and provides evidence for the good quality of the obtained data. Figs 2 and 3 compare the present *A* values for dipole allowed transitions with those from Kurucz & Bell (1995) and NIST for Sc II and Cr II. In comparing our data with Kurucz & Bell one finds the same general trends in the results, despite the observed dispersion. One the other hand, there are significant discrepancies between our results and the data in NIST for Sc II. Particularly suspicious are the highest *gf* values in NIST which appear too large by at least one order of magnitude. Unfortunately, the original publication for these data (Johansson & Litzén 1980) does not list either *A* or *gf* values, thus we do not know whether the errors for these transitions come from there. On the other hand, the NIST data base assigns low accuracy (either D or E) to the values listed.

For the case of Cr II, recent experimental measurements of *f* values were presented by Nilsson et al. (2006). Fig. 4 compares our computed transition rates (*A* values) with those of Nilsson et al. The agreement is satisfactory, with an overall dispersion of 24 per cent.

Our representation of the ion was also used to compute electric quadrupole and magnetic dipole transition rates. The results of such calculations are sensitive to configuration interactions and level mixing. Some previous calculations of forbidden transitions of Sc II were performed by Warner & Kirkpatrick (1969) using a

Table 3. Energy terms in Rydberg for the Sc II ion relative to the ground state. The table compares experimental energies with *ab initio* calculated energies (Theo.¹) and energies with TEC (Theo.²).

| Term | Theo. ¹ | Theo. ² | Exp. | Term | Theo. ¹ | Theo. ² | Exp. |
|-------------------------------------|--------------------|--------------------|---------|-------------------------------------|--------------------|--------------------|---------|
| 3d ² 4s a ⁴ F | 0.00 | 0.0 | 0.0 | 3d ³ a ² P | 0.09824 | 0.08848 | 0.09057 |
| 3d ³ b ⁴ F | 0.02270 | 0.00784 | 0.00992 | 3d ² 4s b ⁴ P | 0.09021 | 0.08878 | 0.09087 |
| 3d ² 4s a ² F | 0.07480 | 0.04153 | 0.04359 | 3d ³ b ² D | 0.15834 | 0.11374 | 0.11580 |
| 3d ² 4s a ² D | 0.08081 | 0.07751 | 0.07956 | 3d ³ a ² H | 0.15813 | 0.11394 | 0.11601 |
| 3d ³ a ² G | 0.10865 | 0.08055 | 0.08261 | 3d ² 4s b ² G | 0.16209 | 0.13702 | 0.13907 |
| 3d ³ a ⁴ P | 0.09021 | 0.08408 | 0.08616 | | | | |

Table 4. Energy terms in Rydberg for the Cr II ion relative to the ground state. The table compares experimental energies with *ab initio* calculated energies (Theo.¹) and energies with TEC (Theo.²).

| Config. | Term | Theo. ¹ | Theo. ² | Exp. | Config. | Term | Theo. ¹ | Theo. ² | Exp. |
|--------------------|-------------------------------|--------------------|--------------------|---------|---------------------------------|-------------------------------|--------------------|--------------------|---------|
| 3d ⁵ | a ⁶ S | 0.00000 | 0.00000 | 0.00000 | 3d ⁴ 4p | z ⁶ D ^o | 0.42239 | 0.45313 | 0.45226 |
| 3d ⁴ 4s | a ⁶ D | 0.10314 | 0.11188 | 0.11188 | 3d ⁴ 4s | c ² G | 0.42563 | 0.36333 | 0.36234 |
| 3d ⁴ 4s | a ⁴ D | 0.19879 | 0.18039 | 0.18069 | 3d ⁴ 4p | z ⁴ P ^o | 0.42649 | 0.44714 | 0.44938 |
| 3d ⁵ | a ⁴ G | 0.21674 | 0.18695 | 0.18695 | 3d ⁵ | c ² F | 0.43579 | 0.36367 | 0.36286 |
| 3d ⁵ | a ⁴ P | 0.24098 | 0.19886 | 0.19887 | 3d ⁴ 4p | z ⁴ F ^o | 0.45548 | 0.47199 | 0.47194 |
| 3d ⁵ | b ⁴ D | 0.27470 | 0.22851 | 0.22818 | 3d ⁴ 4s | b ² D | 0.45752 | 0.39112 | 0.39124 |
| 3d ⁴ 4s | a ⁴ H | 0.30386 | 0.27594 | 0.27597 | 3d ⁴ 4s | c ² D | 0.48500 | 0.41448 | 0.41650 |
| 3d ⁵ | a ² I | 0.31431 | 0.27469 | 0.27472 | 3d ³ 4s ² | c ⁴ F | 0.48929 | 0.48805 | 0.48805 |
| 3d ⁴ 4s | a ⁴ F | 0.31767 | 0.28147 | 0.28398 | 3d ⁴ 4p | z ⁴ D ^o | 0.49021 | 0.49797 | 0.49795 |
| 3d ⁴ 4s | b ⁴ P | 0.31926 | 0.27814 | 0.27818 | 3d ⁵ | b ² S | 0.49148 | 0.40488 | 0.40376 |
| 3d ⁴ 4s | b ⁴ G | 0.34342 | 0.30589 | 0.30608 | 3d ⁵ | d ² D | 0.51745 | 0.43420 | 0.43159 |
| 3d ⁵ | a ² D | 0.34422 | 0.28706 | 0.28635 | 3d ⁴ 4s | d ² F | 0.53938 | 0.46178 | 0.46179 |
| 3d ⁵ | b ⁴ F | 0.34853 | 0.30147 | 0.29933 | 3d ⁵ | d ² G | 0.54633 | 0.47692 | 0.47669 |
| 3d ⁵ | a ² F | 0.35611 | 0.29621 | 0.29581 | 3d ⁴ 4p | z ⁴ H ^o | 0.57728 | 0.58154 | 0.58165 |
| 3d ⁴ 4s | a ² H | 0.36214 | 0.30876 | 0.31648 | 3d ⁴ 4s | c ⁴ P | 0.59072 | 0.50390 | 0.50346 |
| 3d ⁴ 4s | b ² F | 0.37401 | 0.32347 | 0.32433 | 3d ⁴ 4s | d ⁴ F | 0.59416 | 0.50015 | 0.50007 |
| 3d ⁴ 4s | a ² P | 0.37737 | 0.32016 | 0.32007 | 3d ⁴ 4p | y ⁴ D ^o | 0.59536 | 0.58773 | 0.58774 |
| 3d ⁵ | a ² G | 0.37870 | 0.32944 | 0.32985 | 3d ⁴ 4p | z ⁴ I ^o | 0.59855 | 0.59737 | 0.59738 |
| 3d ⁵ | b ² H | 0.38155 | 0.33312 | 0.32499 | 3d ⁴ 4p | z ⁴ G ^o | 0.60064 | 0.59616 | 0.59621 |
| 3d ⁴ 4s | c ⁴ D | 0.39722 | 0.34914 | 0.34915 | 3d ⁴ 4p | z ² G ^o | 0.60251 | 0.59804 | 0.59797 |
| 3d ⁴ 4p | z ⁶ F ^o | 0.39761 | 0.43154 | 0.43155 | 3d ⁴ 4p | z ² S ^o | 0.60905 | 0.59288 | 0.59259 |
| 3d ⁴ 4s | b ² G | 0.40628 | 0.35119 | 0.35119 | 3d ³ 4s ² | d ⁴ P | 0.60933 | 0.60234 | 0.60246 |
| 3d ⁴ 4p | z ⁶ P ^o | 0.40877 | 0.44219 | 0.44227 | 3d ⁴ 4p | y ⁴ G ^o | 0.61804 | 0.61369 | 0.61376 |
| 3d ⁴ 4s | b ² I | 0.41356 | 0.36650 | 0.36646 | 3d ⁴ 4p | y ⁴ P ^o | 0.61928 | 0.60606 | 0.60622 |
| 3d ⁴ 4s | a ² S | 0.42119 | 0.36731 | 0.36829 | 3d ⁴ 4p | y ⁴ F ^o | 0.62302 | 0.61311 | 0.61315 |

single configuration approximation with empirical Slater parameters and more recently by Lundin et al. (2008) using the *civ3* code. Their values are compared with our present results in Table 5. The agreement between the present results with the calculations of Lundin et al. is remarkable for most transitions, with the exception of 3d² ³F₄–3d4 s³ D₃ and 3d² ³P₁–3d4s ³D₂ transitions and some weak transitions from the 3d² ¹G₄ level. For the former two transitions the differences are almost exactly a factor of 10, which suggest that could come from typographical errors in the tabulation. On the other hand, transitions from the 3d² ¹G₄ level are dominated by that to 3d4s¹D₂ and for this the difference is only 10 per cent. Moreover, the lifetime of 2.59 s for the 3d² ¹G₄ level derived from our calculations agrees better with the experimental value of (2.64 ± 0.18) s than the calculated 2.841 s value of Lundin et al. Despite these scattered differences we conclude that the present radiative data base for [Sc II] is reliable for our spectral modelling.

Table 6 presents a comparison between the present transition rates for forbidden transitions to the ground level of Cr II and previous calculations by Nussbaumer & Swings (1970), using single configuration line strengths provided by Garstang (1957, 1958, 1964).

The lack of configuration interaction in their calculation yields inaccurate results for various transitions.

2.2 Collisional data for Sc II and Cr II

We have computed electron impact collision strengths for transitions among the lowest 30 energy levels of Sc II that belong to the configurations 3d², 3d4s, 3d4p and 4s², and 162 levels of Cr II that belong to the configurations 3d⁴, 3d³4s, 3d³4p and 3d²4s². We employ the Breit–Pauli R-matrix (BPRM) method and the BPRM set of codes developed in the framework of the IRON Project (Hummer et al. 1993; Berrington et al. 1995). The calculations include partial wave contributions with angular momentum $L = 0–10$. Then, the collision strengths were ‘topped up’ with estimates of contributions from higher partial waves based on the Coulomb–Bethe approximation (Burgess 1974). Collision strengths for the fine-structure levels were obtained by algebraic recoupling of the LS reactance matrices (Hummer et al. 1993). Figs 5 and 6 show collision strengths for some of the dominant transitions in Sc II and Cr II, respectively.

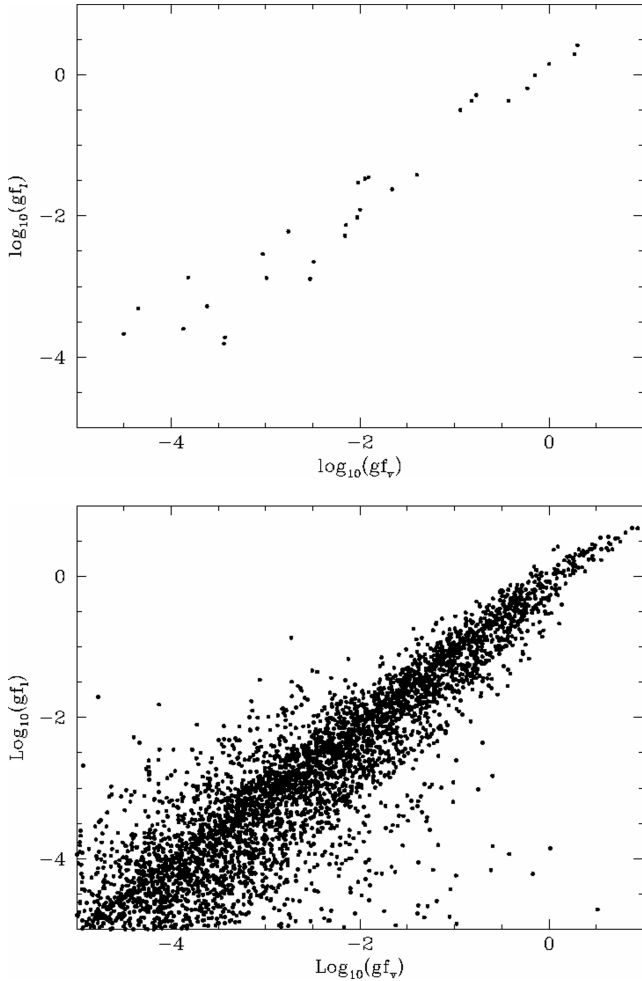


Figure 1. $\log(gf)$ values calculated in their velocity gauge plotted against those in the length gauge for dipole allowed transitions calculated for Sc II (upper) and Cr II (lower).

We compute Maxwellian averaged effective collision strengths, defined as

$$\Upsilon(T) = \int_0^{\infty} \Omega_{if}(\epsilon_f) \exp(-\epsilon_f/kT) d(\epsilon_f/kT), \quad (3)$$

where Ω_{if} is the collision strength for the transition i to f , and ϵ_f is the energy of the outgoing electron. The Υ s were computed for various temperatures between 2000 and 30 000 K.

2.3 Multilevel model of Sc II and Cr II

We build multilevel excitation equilibrium models for Sc II and Cr II which consider electron impact excitation and continuum fluorescence excitation (see Bautista, Peng & Pradhan 1996). We assume that the radiation field density, U_ν , at photon energies below the Lyman ionization limit (13.6 eV) can be approximated by a blackbody with temperature T_R times a geometrical dilution factor w , i.e.

$$\frac{c^3 U_\nu}{8\pi h \nu^3} = \frac{w}{\exp(h\nu/kT_R) - 1}.$$

For the present calculations we adopt a temperature of 35 000 K as in previous calculations of Bautista et al. (2002, 2006). We decided to use this simple blackbody spectrum for the lack of enough understanding of the actual spectrum that heats the filament. Although,

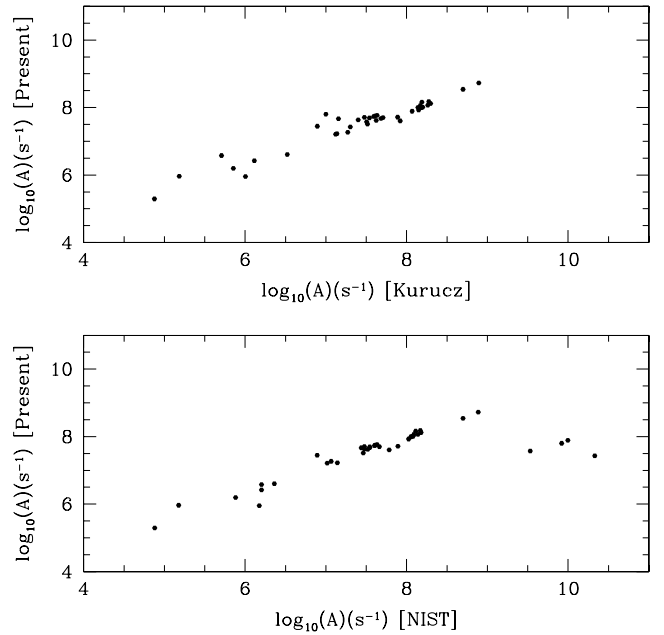


Figure 2. $\log(A)$ from present calculations plotted against $\log(A)$ from Kurucz (1995; upper panel) and NIST (lower panel) for dipole allowed transitions calculated for Sc II.

we see some continuum along our line of sight, this is likely very different from that reaching the filament. As Fe is mostly neutral in the filament while other species are ionized indicates that there is a substantial shielding by Fe along that sight line which is not present along our line of sight. There are also issues with scattering and dust extinction, which is known to be very patchy throughout the nebula. Thus, we see no gain in using the observed continuum at this point and prefer to use the simplest model. The nature of the continuum that heats the filament is a subject of interest for further research.

Grotrian diagrams for Sc II and Cr II are presented in Figs 7 and 8. These diagrams show the main lines identified in our spectra of the Sr filament. It can be seen that many optical and ultraviolet (UV) lines arise from levels located several eV above the ground state. Such levels could not be efficiently populated by electronic collisions. Instead, the spectra are driven by a combination of collisional excitation and photoexcitation by continuum radiation (see Bautista et al. 2004, 2006).

Bautista et al. (2002) estimated an upper bound for the dilution factor for the strontium filament of $\sim 10^{-9}$.

3 SPECTRAL DIAGNOSTICS

We use the [Sc II] and [Cr II] lines in the spectra to diagnose the physical conditions of the filament. Previous diagnostics were reported in Bautista et al. (2002) from the [Sr II] lines and in Bautista et al. (2006) from [Ni II] and [Ti II]. There, we estimated an electron density of the order of 10^7 cm^{-3} , a temperature of $7000 \pm 1000 \text{ K}$ and a dilution factor for photoexcitation between $\sim 10^{-10}$ and $\sim 10^{-9}$.

3.1 Observed line intensities

The spectra used in the present work were observed by the *HST* and its STIS during 2001 November. The $52 \times 0.2 \text{ arcsec}^2$ aperture was oriented almost along the axis of the Homunculus at a position angle

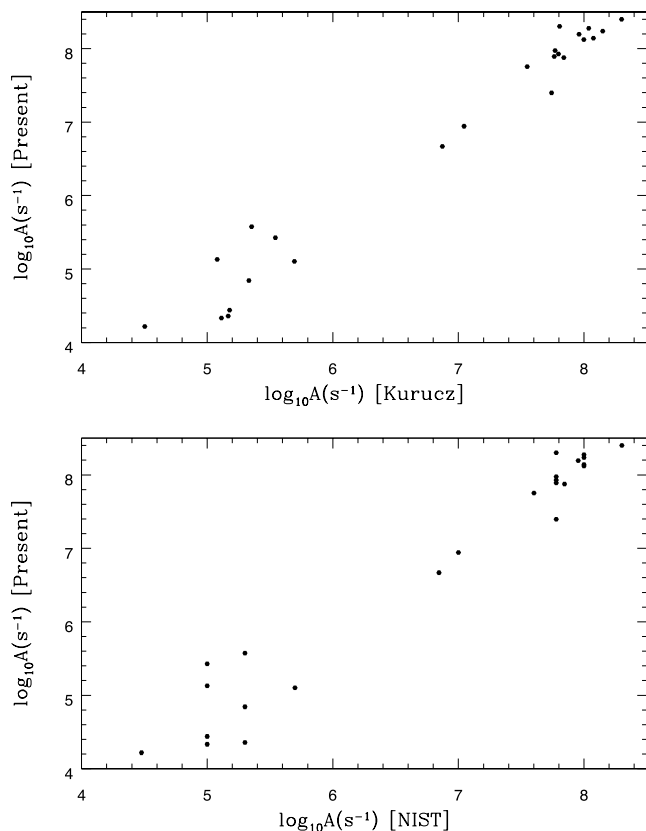


Figure 3. $\log(A)$ from present calculations plotted against $\log(A)$ from Kurucz (1995; upper panel) and NIST (lower panel) for dipole allowed transitions calculated for Cr II.

of -130° . These spectra are described in more detail in Hartman et al. (2004). We extracted a 0.25-arcsec long portion of the spectrum at the peak of the Sr filament located at a projected angular distance of 2 arcsec from the star, the same region analysed in previous papers discussing properties of Sr II, Ti II and Ni II (Bautista et al. 2002, 2006).

The filament was observed at a number of spectral intervals in the near UV through near red at additional position angles, largely determined by the *HST* spacecraft constraints at each time of observation. We were able to learn substantially more about the velocity structure in line of sight using spectra recorded at identical grating settings, but at different position angles. From these data we identified a major velocity component, at around -100 km s^{-1} seen uniquely in the Sr II and Ti II lines. Other, but not all, elements have an additional, but weaker, component at around -160 km s^{-1} . In this and previous papers we chose to analyse only the -100 km s^{-1} component as it is common to all elements and thereby we could obtain abundance ratios. In the 2001 November data, lines having several velocity components were fitted by two Gaussians with centre velocities fixed at -100 and -160 km s^{-1} , respectively. As these lines are marginally resolved, our flux measures for each component are naturally less certain than for the single-component lines. The Cr II lines were fitted with two components, allowing us to derive the contribution from the -100 km s^{-1} component. The Sc II lines are weaker, but the velocities of the lines are consistent with a single component at -100 km s^{-1} .

The complete list of lines used for the present study and their intensities, corrected for extinction is presented in Table 7. It is

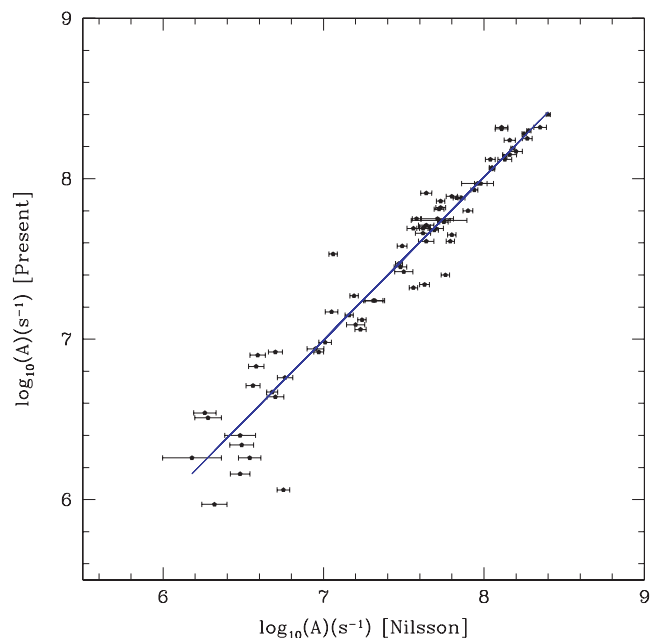


Figure 4. $\log(A)$ from present calculations plotted against experimental values from Nilsson et al. (2006).

important to point out that many more lines were identified, but only for the ones tabulated here their fluxes could be accurately measured. For the visual extinction magnitude we use the same value, $A_V = 2.1$, as in the previous study of Ni II and Ti II emission. The extinction curve used was that of Cardelli, Clayton & Mathis (1989).

3.2 Diagnostics

Fig. 9 shows various emissivity line ratios among forbidden lines of Sc II against the logarithm of the dilution factor (w). Here, the ratios are computed for three different electron densities 10^6 , 10^7 and 10^8 cm^{-3} and three different temperatures, i.e. 6000, 7000 and 8000 K. The line ratios are potentially useful as diagnostics of physical conditions, although the large uncertainties in the measured fluxes prevent us from deriving firm conclusions. On the other hand, combinations of forbidden lines in the near-infrared part of the spectrum and dipole allowed lines in the optical might seem to be good diagnostics. However, it was found that both types of lines could not be reproduced simultaneously; the dipole allowed lines were too strong with respect to forbidden lines for any set of physical conditions. We interpret this problem as a result of two effects: (1) there is large uncertainty in the true reddening curve for the observed region which yields errors whenever working with lines with very different wavelengths; (2) it seems likely that dipole and forbidden lines arise from different spatial regions. Bautista et al. (2004) showed that the physical conditions vary widely within the area covered by our observations. Thus, it is possible that dipole allowed lines that are excited by continuum fluorescence may arise from a different spatial region than forbidden lines, which require combined contributions of photoexcitation and electron impact excitation in high density regions.

Table 8 compares the relative intensities of [Sc II] and Sc II lines, respectively, with theoretical predictions. For convenience, we normalize all the line intensities to that of the strongest line in the spectrum, and presumably the most accurately measured.

Table 5. Comparison between radiative rates (in s^{-1}) for forbidden transitions in Sc II from experimental values from Hartman et al. (2008; Exp.), calculations of Warner & Kirkpatrick (1969; W&K), Lundin et al. (2008; Lundin) and the present work.

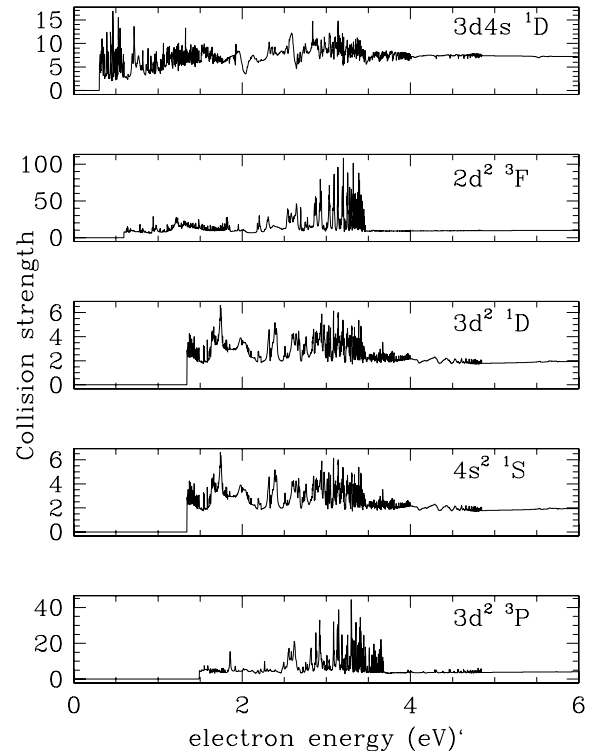
| Levels | Configurations | Terms | $J_i - J_k$ | Wavelength (\AA) | Exp. | W&K | Lundin | Present | |
|--------|----------------|-----------------------|-------------|-----------------------------|----------|------------|--------|---------|---------|
| 1 | 5 | $3p^6 3d4s-3p^6 3d^2$ | $^3D-^3F$ | 1-2 | 20820.9 | | 5.0E-3 | 3.63E-3 | 3.53E-3 |
| 2 | 5 | $3p^6 3d4s-3p^6 3d^2$ | $^3D-^3F$ | 2-2 | 21118.7 | | 3.4E-3 | 2.40E-3 | 2.35E-3 |
| 3 | 5 | $3p^6 3d4s-3p^6 3d^2$ | $^3D-^3F$ | 3-2 | 21621.1 | | 3.0E-4 | 2.12E-4 | 2.09E-4 |
| 1 | 6 | $3p^6 3d4s-3p^6 3d^2$ | $^3D-^3F$ | 1-3 | 20476.8 | | 2.0E-3 | 1.41E-3 | 1.37E-3 |
| 2 | 6 | $3p^6 3d4s-3p^6 3d^2$ | $^3D-^3F$ | 2-3 | 20764.8 | | 4.6E-3 | 3.28E-3 | 3.19E-3 |
| 3 | 6 | $3p^6 3d4s-3p^6 3d^2$ | $^3D-^3F$ | 3-3 | 21250.3 | | 2.5E-3 | 1.75E-3 | 1.71E-3 |
| 5 | 6 | $3p^6 3d^2-3p^6 3d^2$ | $^3F-^3F$ | 2-3 | 1239150 | | 1.4E-5 | 1.36E-5 | 1.35E-5 |
| 2 | 7 | $3p^6 3d4s-3p^6 3d^2$ | $^3D-^3F$ | 2-4 | 20324.9 | | 1.7E-3 | 1.21E-3 | 1.19E-3 |
| 3 | 7 | $3p^6 3d4s-3p^6 3d^2$ | $^3D-^3F$ | 3-4 | 20789.9 | | 2.6E-3 | 5.42E-4 | 5.29E-3 |
| 6 | 7 | $3p^6 3d^2-3p^6 3d^2$ | $^3F-^3F$ | 3-4 | 959500 | | 2.3E-5 | 2.30E-5 | 2.29E-5 |
| 2 | 10 | $3p^6 3d4s-3p^6 3d^2$ | $^3D-^3P$ | 2-0 | 8326.62 | 0.75(0.08) | 8.8E-1 | 6.66E-1 | 6.36E-1 |
| 5 | 10 | $3p^6 3d^2-3p^6 3d^2$ | $^3F-^3P$ | 2-0 | 13749.07 | | 5.3E-2 | 3.02E-2 | 3.00E-2 |
| 1 | 11 | $3p^6 3d4s-3p^6 3d^2$ | $^3D-^3P$ | 1-1 | 8261.17 | 0.34(0.08) | 4.1E-1 | 3.12E-1 | 2.98E-1 |
| 2 | 11 | $3p^6 3d4s-3p^6 3d^2$ | $^3D-^3P$ | 2-1 | 8307.66 | | 7.4E-2 | 5.57E-2 | 5.00E-1 |
| 3 | 11 | $3p^6 3d4s-3p^6 3d^2$ | $^3D-^3P$ | 3-1 | 8384.33 | 0.28(0.06) | 4.0E-1 | 3.00E-1 | 2.95E-1 |
| 5 | 11 | $3p^6 3d^2-3p^6 3d^2$ | $^3F-^3P$ | 2-1 | 13697.46 | | 1.8E-2 | 1.03E-2 | 1.02E-2 |
| 6 | 11 | $3p^6 3d^2-3p^6 3d^2$ | $^3F-^3P$ | 3-1 | 13850.6 | | 3.4E-2 | 1.95E-2 | 1.93E-2 |
| 1 | 11 | $3p^6 3d^2-3p^6 3d^2$ | $^3P-^3P$ | 0-1 | 3649600 | | 3.7E-7 | 3.71E-7 | 3.68E-7 |
| 1 | 12 | $3p^6 3d4s-3p^6 3d^2$ | $^3D-^3P$ | 1-2 | 8225.2 | | 8.4E-2 | 6.36E-2 | 6.07E-2 |
| 2 | 12 | $3p^6 3d4s-3p^6 3d^2$ | $^3D-^3P$ | 2-2 | 8271.28 | 0.24(0.05) | 3.2E-1 | 2.39E-1 | 2.29E-1 |
| 3 | 12 | $3p^6 3d4s-3p^6 3d^2$ | $^3D-^3P$ | 3-2 | 8347.28 | 0.51(0.09) | 4.9E-1 | 3.66E-1 | 3.51E-1 |
| 5 | 12 | $3p^6 3d^2-3p^6 3d^2$ | $^3F-^3P$ | 2-2 | 13598.86 | | 1.6E-3 | 9.50E-4 | 9.23E-4 |
| 6 | 12 | $3p^6 3d^2-3p^6 3d^2$ | $^3F-^3P$ | 3-2 | 13749.79 | | 1.1E-2 | 6.08E-3 | 6.01E-3 |
| 7 | 12 | $3p^6 3d^2-3p^6 3d^2$ | $^3F-^3P$ | 4-2 | 13949.75 | | 3.8E-2 | 2.17E-2 | 2.15E-2 |
| 1 | 12 | $3p^6 3d^2-3p^6 3d^2$ | $^3P-^3P$ | 1-2 | 1889600 | | 2.0E-6 | 1.99E-6 | 1.99E-6 |
| 2 | 13 | $3p^6 3d4s-3p^6 3d^2$ | $^3D-^1G$ | 2-4 | 7043.49 | | 2.2E-3 | 1.27E-3 | 6.46E-4 |
| 3 | 13 | $3p^6 3d4s-3p^6 3d^2$ | $^3D-^1G$ | 3-4 | 7098.52 | | 5.1E-5 | 5.56E-5 | 3.76E-4 |
| 6 | 13 | $3p^6 3d^2-3p^6 3d^2$ | $^3F-^1G$ | 3-4 | 10660.62 | | 5.3E-4 | 7.41E-4 | 5.32E-4 |
| 7 | 13 | $3p^6 3d^2-3p^6 3d^2$ | $^3F-^1G$ | 4-4 | 10780.43 | | 8.5E-4 | 1.19E-3 | 8.83E-4 |

Table 6. Comparison between radiative rates (in s^{-1}) for forbidden transitions in Cr II from Nussbaumer & Swings (1970; N&S) and the present work.

| Wavelength (\AA) | Configurations | Terms | $J_i - J_k$ | N&S | Present |
|-----------------------------|--------------------|-------------|-------------|--------|---------|
| 8002.28 | $3d^5-3d^4(^5D)4s$ | a^6S-a^6D | 5/2-9/2 | 1.0E-1 | 1.05E-1 |
| 8127.53 | $3d^5-3d^4(^5D)4s$ | a^6S-a^6D | 5/2-7/2 | 9.4E-2 | 9.74E-2 |
| 8231.93 | $3d^5-3d^4(^5D)4s$ | a^6S-a^6D | 5/2-5/2 | 8.8E-2 | 9.14E-2 |
| 8310.77 | $3d^5-3d^4(^5D)4s$ | a^6S-a^6D | 5/2-3/2 | 8.4E-2 | 8.71E-2 |
| 8359.94 | $3d^5-3d^4(^5D)4s$ | a^6S-a^6D | 5/2-1/2 | 8.2E-2 | 8.46E-2 |
| 4582.42 | $3d^5-3d^5$ | a^6S-a^4P | 5/2-5/2 | 8.0E-2 | 2.62E-1 |
| 4582.09 | $3d^5-3d^5$ | a^6S-a^4P | 5/2-3/2 | 7.0E-2 | 1.69E-1 |
| 3337.71 | $3d^5-3d^5$ | a^6S-b^4P | 5/2-1/2 | 1.0E-2 | 2.60E-4 |

Reasonably good agreement is found between the measured and predicted [Sc II] lines. Though, as discussed above, the relative strength of the optical dipole allowed lines could not be reproduced. Furthermore, for the remain of the analysis we will work with forbidden lines only, which are consistent with the conditions derived previously with other species (Bautista et al. 2004).

Unfortunately, all the [Cr II] lines measured arise from the a^6D multiplet whose levels are thermalized among them by rapid collisional transitions. Other lines from the a^4P multiplet would have been useful as diagnostics, but despite being observed they could not be deblended from an additional kinematic system in the ejecta. The measured and predicted [Cr II] lines, normalized to the strongest line measured [$\lambda 8231.93$], are compared in Table 9. As explained

**Figure 5.** Collision strengths versus incident electron energy for excitations from the ground level $3d4s^3D$ to the first five excited configurations of Sc II.

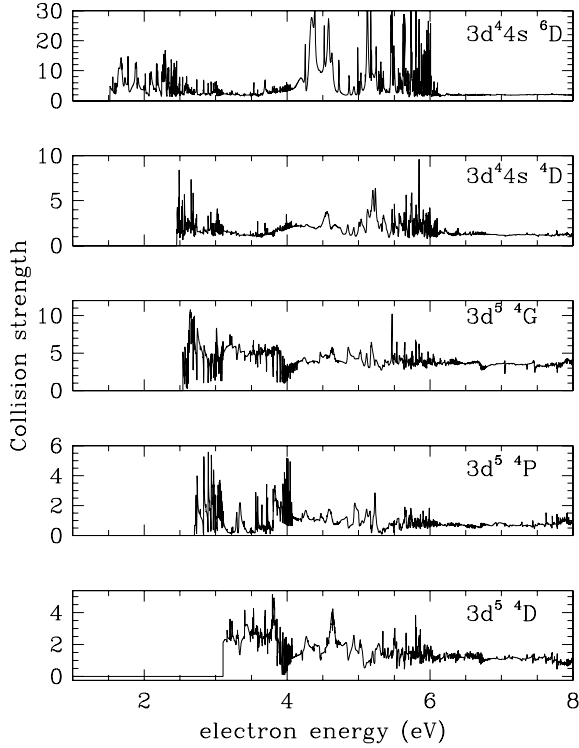


Figure 6. Collision strengths versus incident electron energy for excitations from the ground level a^6S to the first five excited configurations of Cr II.

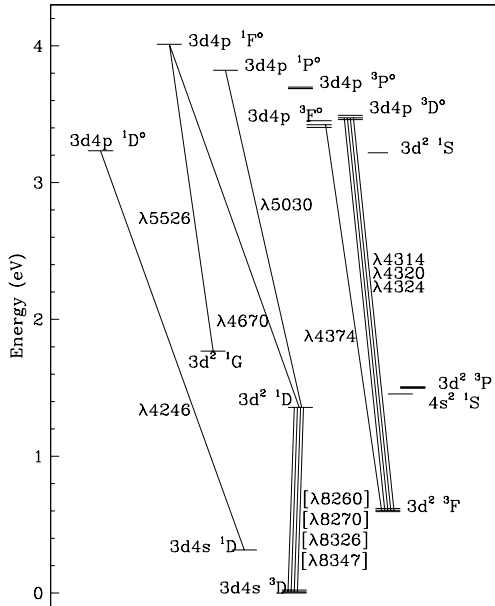


Figure 7. Partial Grotrian diagram of Sc II showing lines observed in the filament.

above, the theoretical relative intensities are nearly independent of the physical conditions. One can see that there is good agreement between theory and observations for the relative intensities of the $[\lambda 8231.93]$, $[\lambda 8310.77]$ and $[\lambda 8359.94]$ lines. By contrast, the measured intensities for the $[\lambda 8002.28]$ and $[\lambda 8127.53]$ lines are much lower than predicted. These discrepancies are difficult to understand in terms of the atomic model and could be due systematic errors in

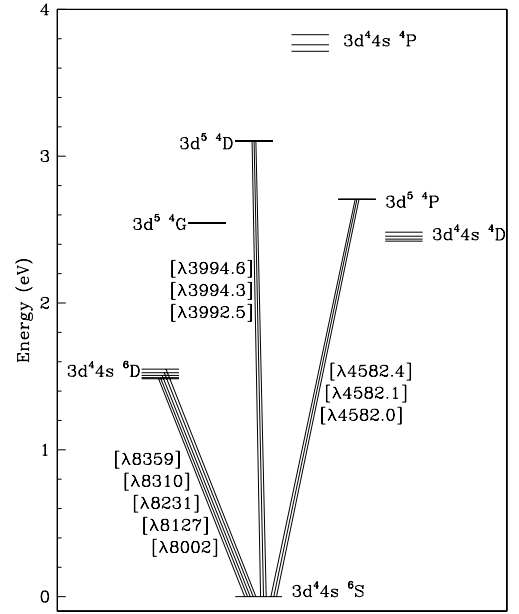


Figure 8. Partial Grotrian diagram of Cr II showing lines observed in the filament.

Table 7. Observed (I_{obs}) and reddening corrected line fluxes (I_{cor}) of the Sc II and Cr II lines from the Sr filament of η Carinae. The laboratory wavelengths are in air. The uncertainties in the measured fluxes are estimated in 10 per cent for all lines.

| Line | Transition | I_{obs} | I_{cor}^a |
|---------------------|---------------------------|------------------|--------------------|
| [Sc II] lines | | | |
| $[\lambda 8261.17]$ | $a^3D_1 - a^3P_1$ | 1.8 | 5.5 |
| $[\lambda 8271.28]$ | $a^3D_2 - a^3P_2$ | 2.7 | 8.2 |
| $[\lambda 8326.62]$ | $a^3D_2 - a^3P_0$ | 1.7 | 5.4 |
| $[\lambda 8347.28]$ | $a^3D_3 - a^3P_2$ | 5.6 | 16 |
| $[\lambda 8384.33]$ | $a^3D_3 - a^3P_1$ | 1.5 | 4.8 |
| Sc II lines | | | |
| $\lambda 4315.30$ | $a^3F_4 - z^3D_3$ | 30 | 410 |
| $\lambda 4321.95$ | $a^3F_3 - z^3D_2$ | 27 | 370 |
| $\lambda 4326.21$ | $a^3F_2 - z^3D_1$ | 26 | 360 |
| $\lambda 4375.69$ | $a^3F_4 - z^3F_4$ | 15 | 200 |
| $\lambda 4671.71$ | $b^1D_2 - z^1F_3$ | 3.9 | 43 |
| $\lambda 5032.42$ | $b^1D_2 - z^1P_1$ | 4.5 | 40 |
| $\lambda 5659.47$ | $a^3P_2 - z^3P_2$ | | |
| | $a^3P_0 - z^1P_2$ | 8.9 | 58 |
| [Cr II] lines | | | |
| $[\lambda 8002.28]$ | $a^6S_{5/2} - a^6D_{9/2}$ | 18 | 57 |
| $[\lambda 8127.53]$ | $a^6S_{5/2} - a^6D_{7/2}$ | 27 | 83 |
| $[\lambda 8231.93]$ | $a^6S_{5/2} - a^6D_{5/2}$ | 30 | 89 |
| $[\lambda 8310.77]$ | $a^6S_{5/2} - a^6D_{3/2}$ | 19 | 56 |
| $[\lambda 8359.94]$ | $a^6S_{5/2} - a^6D_{1/2}$ | 12 | 35 |

^a 10^{-13} erg s $^{-1}$ cm $^{-2}$ arcsec $^{-1}$.

the measurements, as the observed lines had to be debled from a faster kinematic component. We test this hypothesis by comparing the relative intensities of the total integrated lines with models and in this case the $[\lambda 8127.53]$ line agrees well with theoretical predictions. However, the intensity of the $[\lambda 8002.28]$ line is only 60 per cent of the expected value. Comparison of all the lines in velocity space does show that the $[\lambda 8002.28]$ line has a significantly weaker -160 km s $^{-1}$ component than the rest of the lines.

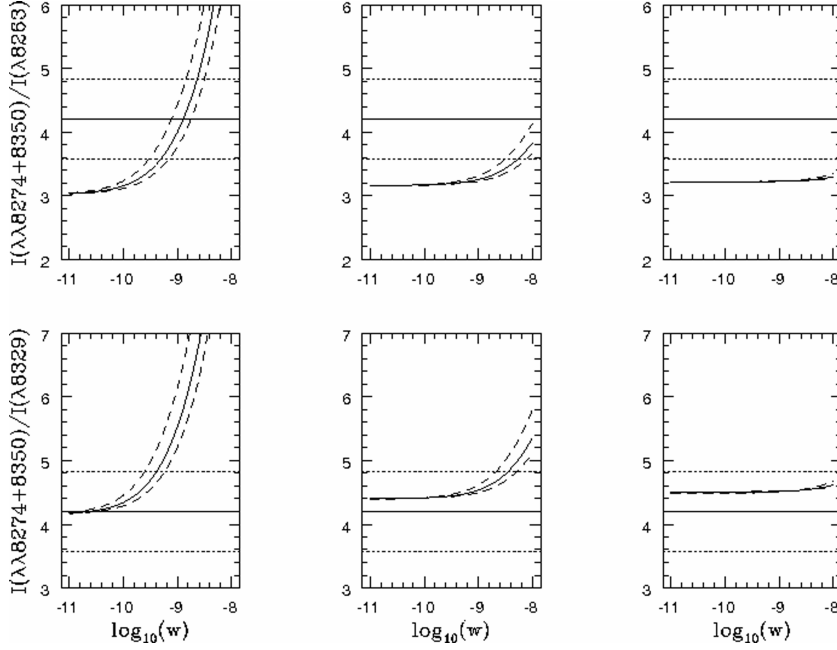


Figure 9. [Sc II] emissivity line ratios against the logarithm of the dilution factor. The curves were computed for $N_e = 10^6$ (left-hand column), 10^7 (middle column) and 10^8 cm^{-3} (right-hand column), and $T_e = 6000$ (dotted line), 7000 (dashed line) and 6000 K (solid line). The solid horizontal lines indicate the observed lines ratios and the dashed lines indicate errors.

Table 8. Comparison between observed and theoretical line intensities for the Sc II and [Sc II] spectra. Line intensities are relative to $I([\lambda 8261.17])$ and the error in the measurements is estimated in 20 per cent. The theoretical spectrum was computed for $T_e = 6000 \text{ K}$ in all cases and $(\log_{10} w, N_e) = (-9.0, 10^7 \text{ cm}^{-3})$ in (a), $(-9.0, 10^6 \text{ cm}^{-3})$ in (b), $(-8.3, 10^7 \text{ cm}^{-3})$ in (c).

| Line | $I(\lambda)/I(\lambda 4315)$ | | | |
|---------------------|------------------------------|------|------|------|
| | Obs. | (a) | (b) | (c) |
| $[\lambda 8261.17]$ | 1.0 | 1.0 | 1.0 | 1.0 |
| $[\lambda 8271.28]$ | 1.5 | 1.3 | 1.6 | 1.4 |
| $[\lambda 8326.62]$ | 0.94 | 0.72 | 0.72 | 0.72 |
| $[\lambda 8347.28]$ | 3.1 | 2.0 | 2.4 | 2.2 |
| $[\lambda 8384.33]$ | 0.87 | 0.96 | 0.96 | 0.96 |
| $\lambda 4315.30$ | 68 | 5.1 | 16 | 22 |
| $\lambda 4321.95$ | 62 | 3.7 | 11 | 15 |
| $\lambda 4326.21$ | 60 | 2.4 | 7.4 | 10 |
| $\lambda 4375.69$ | 33 | 2.5 | 8.0 | 11 |
| $\lambda 4671.71$ | 7.2 | 0.60 | 1.8 | 2.6 |
| $\lambda 5032.42$ | 7.2 | 0.76 | 2.1 | 3.0 |
| $\lambda 5659.47$ | 10 | 0.69 | 2.2 | 3.0 |

4 THE Sc AND Cr ABUNDANCES IN THE Sr FILAMENT

Using the physical conditions determined above we proceed to compute the relative abundances of Sc II and Cr II.

From the present lines and those of [Ni II] from Bautista et al. (2004) we derive $N(\text{Sc II})/N(\text{Ni II}) = 0.03$ and $N(\text{Cr II})/N(\text{Ni II}) = 0.06$. The uncertainty is conservatively estimated about a factor of 2 from the intrinsic uncertainties of spectral models, flux measurements and observed scatter between theoretical and observed line intensities. This uncertainty estimate takes into account the dispersion between all the lines in the spectrum, an uncertainty in the physical conditions and the atomic data.

Table 9. Comparison between observed and theoretical line intensities for the [Cr II] spectrum. Line intensities are relative to $I([\lambda 8231.93])$ and the error in the measurements is estimated in 20 per cent. The theoretical spectrum was computed for $T_e = 6000 \text{ K}$, $N_e = 10^7 \text{ cm}^{-3}$ and $w = 10^{-9}$.

| Line | $I(\lambda)/I([\lambda 8231])$ | |
|---------------------|--------------------------------|-------|
| | Obs. | Model |
| $[\lambda 8231.93]$ | 1.00 | 1.00 |
| $[\lambda 8002.28]$ | 0.63 | 1.80 |
| $[\lambda 8127.53]$ | 0.91 | 1.38 |
| $[\lambda 8310.77]$ | 0.61 | 0.65 |
| $[\lambda 8359.94]$ | 0.38 | 0.32 |

To estimate the total $N(\text{Sc})/N(\text{Ni})$ and $N(\text{Cr})/N(\text{Ni})$ abundance ratios we notice that these elements are only seen in their singly ionized stages. Only Fe is seen in its neutral stage. As discussed in Bautista et al. (2006), for a temperature between 5000 and 7000 K Ni is expected to be mostly in the Ni II stage, while Fe is mostly in its neutral form Sc and Cr have lower ionization potentials than Ni by 1.1 and 0.9 eV, respectively, which suggests that Sc and Cr should be more ionized than Ni and $N(\text{Sc})/N(\text{Ni}) \geq N(\text{Sc}^+)/N(\text{Ni}^+) = 0.03$ and $N(\text{Cr})/N(\text{Ni}) \geq N(\text{Cr}^+)/N(\text{Ni}^+) = 0.06$ in gas phase. The total uncertainties here are estimated to about a factor of 3. These abundance ratios of Sc and Cr to Ni are about 30 times and 1/4 times the solar ratios of 0.00072 and 0.27, respectively (Lodders 2003).

5 DUST CONDENSATION IN THE STRONTIUM FILAMENT

The observed $\text{Sc}/\text{Ni} \geq 30$ times solar compares well to the $\text{Ti}/\text{Ni} \approx 40$ found earlier (Bautista et al. 2006). By contrast, Cr is clearly much less enriched than Sc and Ti relative to Ni. This can

be explained by the different condensation behaviour of Sc and Ti in contrast to Cr. In a solar composition gas, Sc condenses as Sc_2O_3 into solid solution with Ca-, Al- and Ca–Ti-bearing host minerals. Scandium substitutes for the Ca, Al or Ti in the mineral lattice of these more abundant oxides. On the other hand, Cr condenses into a FeNi alloy.

In η Carinae the chemical composition of the ejecta has been altered by the CNO cycle to create a N-rich, C- and O-poor composition. Under these conditions, Ca–Al and Ca–Ti oxides are unstable. Instead, TiC and/or TiN (osbornite) condense. Here Sc forms a nitride (ScN), and this nitride can condense into solid solution with TiC (as well as TiN). Fe and Ni condense as a silicide alloy (Fe,Ni)Si instead of a metal alloy. Chromium is less refractory and it condenses into solid solution with (Fe,Ni)Si, that condensed at higher temperature.

We adopted the same overall composition for the CNO processed gas as before (Bautista et al. 2006) and calculated the 50 per cent condensation temperatures for Ti, Sc, Cr and Ni. At the 50 per cent condensation temperatures, half of the elements total abundance is in the gas phase and the other half is in condensed phases. These 50 per cent condensation temperatures are useful measures for the volatility fractionation caused by condensation. The 50 per cent condensation temperatures depend on total pressure, but in most cases the relative condensation sequence, which is of most interest here, is not affected. Condensation of TiC (the host for Sc) begins at higher temperatures than the formation of the silicide (≈ 100 K higher; see fig. 11 in Bautista et al. 2006). Here we adopt a nominal total pressure of $1e-7$ bar. The 50 per cent condensation temperatures are 1390 (Ti), 1304 (Sc), 1293 (Ni) and 1100 K (Cr). Thus, for the elements considered here, we have the condensation sequence $\text{Ti} > \text{Sc} > \text{Ni} > \text{Cr}$ with decreasing temperature at constant total pressure.

We now relate the observed abundances to the condensation sequences. The observations are for the gas phase abundances. If originally all elements were in the gas, and the high-temperature gas phase abundances were modified by condensation as the gas cooled, we would expect that the refractory elements (e.g. Ti, Sc) would be more depleted from the gas than the volatile elements (e.g. Cr). This is just the opposite as observed. Therefore, condensation in the ejecta of η Carinae alone cannot have produced the observed abundances. Heating and evaporation of dust containing all previously condensed minerals also does not work. As dust is heated, the more volatile elements (Cr, Ni) are released from the dust first and the more refractory elements (Sc, Ti) last. For partial evaporation under equilibrium conditions, this increases the volatile elements over the refractory elements, again opposite to what is observed in the gas.

We find two possible scenarios related dust formation and destruction that may explain the observed abundances.

- Non-equilibrium condensation in a photoionized plasma. It seems clear that during dust condensation high column densities of H, He and Fe must have shielded the region from radiation more energetic than ~ 8 eV. Thus, most elements recombined and the temperature became low enough for chemical bonding. But, as electron density and temperature dropped most of Fe and Ni would have been in their ground states and there would have been very little opacity for energies below the Fe and Ni ionization thresholds (7.87 and 7.64 eV). However, the first ionization potentials of Sc and Ti are only 6.54 and 6.82 eV, respectively. Then, it is conceivable that significant fractions of these elements would have been photoionized, which would prevent them from condensing. Furthermore, we would expect to see relatively high abundances of these elements

with respect to Fe and Ni, which did condense efficiently. One possible problem with this scenario is that the gas phase abundance of Cr, which also has a low first ionization potential of 6.77 eV, is not enhanced but seems to follow the abundance of Ni. This, perhaps, might be due to efficient condensation of Cr^+ into (Fe,Ni)Si grains as opposed to chemical reactions of Sc and Ti with N and C.

- Preferred evaporation our previous scenario (Bautista et al. 2006) invokes fractional condensation from the ejecta to obtain spatial separation of refractory (TiC) and less refractory dust [(Fe,Ni)Si], and subsequent preferred evaporation of the most refractory dust. In ejecta that cool as a function of distance from the central star, only the most refractory elements can condense closest to the central source. Then TiC and ScN in solid solution would reside closest to the star. Silicides require lower temperatures, so (Fe,Ni)Si (with Cr in solid solution) condenses further away from the star. In order to obtain the observed abundance trends, it is necessary to separate the residual gas from the dust in the expanding ejecta. This may happen if momentum transfer between dust and gas is not effective, because e.g. total pressures are low. If most of the gas and its opacity are gone, stellar radiation may lead to photoevaporation of dust. The refractory dust closest to the star is exposed the most and would be photoevaporated enriching selectively enriching the gas with Ti and Sc. However, since this region is poor in silicide dust, the elemental contributions from silicide evaporation would be small, so that Sc/Ti and Ti/Ni ratios in the gas would be high. Overall, such a scenario may explain why the observed gas abundances mimic those expected for dust by fractional condensation.

It is very desirable to test this scenario with further abundance determinations of elements with different volatilities. For example, suitable elements are Ca and Al, which are expected to condense as CaS and AlN at even lower temperatures than the silicides. Unfortunately, Al has not been detected yet and the [Ca II] lines in our spectra appear blended with strong emission from other kinematic components, as even the relative intensities of the lines are difficult to explain theoretically. Further observational and theoretical work on this subject is needed.

6 CONCLUSIONS AND DISCUSSION

We have studied the Sc II and Cr II spectra of the Sr filament in η Carinae. To this end we computed radiative and electron impact excitation rates for both ions and constructed appropriated spectral models.

The spectral models were employed for diagnosing the physical conditions of the emitting region. The results are consistent with previous determinations using Sr II, [Sr II], [Ti II] and [Ni II] lines (i.e. $N_e \approx 10^7 \text{ cm}^{-3}$, $T_e \approx 7000$ K and a dilution factor between 10^{-10} and 10^{-9}).

We find abundances of Sc and Cr relative to Ni in gas phase of ≥ 30 and $\geq 1/4$ times the solar values. Likewise, a previous study (Bautista et al. 2004) found $N(\text{Ti})/N(\text{Ni})$ 40 times solar.

We study the condensation chemistry of Sc, Cr and Ni in the C- and O-poor and N-rich gas of the ejecta. Then we propose two different mechanisms by which the observed gas phase abundances could be explained. Further observational and theoretical studies are needed to explain discriminate between these models.

ACKNOWLEDGMENTS

We like to thank the anonymous referee for valuable questions and comments that let to material improvements of the paper. The

observations of the strontium filament were made with the STIS on the NASA/ESA *HST* and were obtained by the Space Telescope Science Institute, which is operated by the Association of Universities for Research in Astronomy, Inc., under NASA contract NAS5-26555. HH acknowledges support from the Swedish Research Council (VR). Data for this analysis were gathered under GO programs headed by Kris Davidson and GO and GTO programs headed by Theodore Gull.

REFERENCES

- Badnell N. R., 1986, *J. Phys. B*, 19, 3827
- Bautista M. A., Peng J., Pradhan A. K., 1996, *ApJ*, 460, 372
- Bautista M. A., Gull T. R., Ishibashi K., Hartman H., Davidson K., 2002, *MNRAS*, 331, 875
- Bautista M. A., Hartman H., Gull T. R., Smith N., Lodders K., 2006, *MNRAS*, 370, 1991
- Berrington K. A., Burke P. G., Eissner W., Norrington P. N., 1995, *Comput. Phys. Commun.*, 92, 290
- Burgess A., 1974, *J. Phys. B: At. Mol. Phys.*, 7, L364
- Cardelli J. A., Clayton G. C., Mathis J. S., 1989, *ApJ*, 345, 245
- Damineli A., 1977, in Nota A., Lamer H., ASP Conf. Ser. Vol. 120, *Luminous Blue Variables: Massive Stars in Transition*. Astron. Soc. Pac., San Francisco, p. 272
- Davidson K., Humphreys R., 1997, *ARA&A*, 25, 1
- Davidson K., Dufour R. J., Walborn N. R., Gull T. R., 1986, *ApJ*, 305, 867
- Dufour R. J., Glover T. W., Hester J. J., Currie D. G., van Orsow D., Walter D. K., 1997, in ASP Conf. Ser. Vol. 120. Astron. Soc. Pac., San Francisco, p. 255
- Eissner W., Nussbaumer H., 1969, *J. Phys. B*, 2, 1028
- Eissner W., Jones M., Nussbaumer H., 1974, *Comput. Phys. Commun.*, 8, 270
- Garstang R. H., 1957, *Proc. Cambridge Phil. Soc.*, 53, 214
- Garstang R. H., 1958, *Proc. Cambridge Phil. Soc.*, 54, 383
- Garstang R. H., 1964, *J. Res. N. B. S.*, 68A, 61
- Hartman H., Gull T., Johansson S., Smith N., *HST Eta Carinae Treasury Project Team*, 2004, *A&A*, 419, 215
- Hartman H. et al., 2008, *A&A*, 480, 575
- Hillier D. J., Davidson K., Ishibashi K., Gull T., 2001, *ApJ*, 553, 873
- Hillier D. J. et al., 2006, *ApJ*, 642, 1098
- Hummer D. G., Berrington K. A., Eissner W., Pradhan A. K., Saraph H. E., Tully J. A., 1993, *A&A*, 279, 298
- Ishibashi K. et al., 2003, *AJ*, 125, 3222
- Johansson S., Litzén U., 1980, *Phys. Scr.*, 22, 49
- Kurucz R., Bell B., 1995, Data base at <http://www.pmp.uni-hannover.de/cgi-bin/ssi/test/kurucz/sekur.html>
- Lodders K., 2003, *ApJ*, 591, 1220
- Lundin P., Gurell J., Mannervik S., Royen P., Norlin L.-O., Hartman H., Hibbert A., 2008, *Phys. Scr.*, 78, 015301
- Meynet G., Maeder A., 2002, in Lejeune T., Fernandes J., eds, *ASP Conf. Ser. Vol. 274, Observed HR Diagrams and Stellar Evolution*. Astron. Soc. Pac., San Francisco, p. 17
- Nilsson H., Ljung G., Lundberg H., Nielsen K. E., 2006, *A&A*, 445, 1165
- Nussbaumer H., Swings J. P., 1970, *ApJ*, 162, 589
- Ralchenko Y., Jou F.-C., Kelleher D. E., Kramida A. E., Musgrove A., Reader J., Wiese W. L., Olsen K., 2007, *NIST Atomic Spectra Database*, version 3.1.2. National Institute of Standards and Technology, Gaithersburg, MD. Available at <http://physics.nist.gov/asd3>
- Smith N., Davidson K., Gull T. R., Ishibashi K., Hillier D. J., 2003, *ApJ*, 586, 432
- Verner E. M., Gull T. R., Bruhweiler F., Johansson S., Ishibashi K., Davidson K., 2002, *ApJ*, 581, 1154
- Verner E. M., Bruhweiler F., Bull T., 2005, *ApJ*, 624, 973
- Warner B., Kirkpatrick R. C., 1969, *MNRAS*, 144, 397
- Williams R. E., 1987, *ApJ*, 320, L117
- Zethson T., Gull T. R., Hartman H., Johansson S., Davidson K., Ishibashi K., 2001, *AJ*, 122, 322

This paper has been typeset from a $\text{\TeX}/\text{\LaTeX}$ file prepared by the author.